High cycle fatigue strength of permanent mold and rheocast aluminum 357 alloy

Brochu, Myriam; Verreman, Yves; Ajersch, Frank; Bouchard, Dominique

Publisher's version / Version de l'éditeur:
https://doi.org/10.1016/j.ijfatigue.2010.01.001
International Journal of Fatigue, 32, 8, pp. 1233-1242, 2010-01-18

International Journal of Fatigue 32 (2010) 1233–1242

Contents lists available at ScienceDirect

International Journal of Fatigue

journal homepage: www.elsevier.com/locate/ijfatigue

High cycle fatigue strength of permanent mold and rheocast aluminum 357 alloy

Myriam Brochu [a,*], Yves Verreman [a], Frank Ajersch [a], Dominique Bouchard [b]

[a] École Polytechnique de Montréal, C.P. 6079, Succ. Centre-Ville, Montréal, Qc, Canada H3C 3A7
[b] Centre des Technologies de l'Aluminium, 501, Boul. de l'Université Est, Saguenay, Qc, Canada G7H 8C3

A R T I C L E I N F O

Article history:
Received 1 December 2009
Received in revised form 6 January 2010
Accepted 11 January 2010
Available online 18 January 2010

Keywords:
Aluminum 357 alloy
Casting
Semi-solid molding
High cycle fatigue
Microstructure

A B S T R A C T

The high cycle fatigue resistances of aluminum–silicium–magnesium 357 alloy prepared by semi-solid forming (SSM) and conventional permanent mold casting (PM) are compared under fully reversed loading. Results, reported in *S–N* diagrams, show that rheocasting improves the as-cast alloy mean fatigue strength, by 36% at 10^7 cycles. Part of this improvement is explained by the fact that more SSM specimens are defect free than PM specimens. Comparison of the *S–N* diagrams also reveals that precipitation hardening slightly increases the fatigue strengths of the PM and SSM alloys, and that eutectic modification has no effect on the fatigue performance of the SSM alloy. Observation of small cracks using replicas shows the existence of crack growth decelerations at grain boundaries. No similar decelerations are observed when the crack enters a new α-Al cell within a grain. According to these results, it is proposed that in the absence of defects, the fatigue strength of aluminum alloy 357 is a function of the grain size (D) rather than of the secondary dendrite arm spacing (SDAS) or the spherical diameter of the alpha phase globules (φ_{sph}). Thus, it is concluded that the fatigue strength improvement of the SSM alloy is also related to the smaller grain of the rheocast specimens.

1. Introduction

The fatigue behaviour of conventionally cast (liquid state casting) Al–7%Si–Mg alloys (356 and 357) has been studied by many authors. Most of the experimental work published consists of the generation of *S–N* graphs and the characterization of crack propagation behaviour. Results available in the open literature lead to the following conclusions. The fatigue strength, at 10^7 cycles, of Al–7%Si–Mg for a T6 temper specimen can vary between 60 MPa [1] and 120 MPa [2]. Casting defects have a significant influence on the alloy fatigue strength [3–7]. The defect content, size and nature is known to be influenced by the casting process and the casting conditions that consequently have an effect on the alloy fatigue strength [8–10]. For example, hot isostatic pressing significantly improves the cast alloy fatigue life because it closes or suppresses volumetric defects such as shrinkage cavities and gas pores [6]. Semi-solid molding has a similar effect on fatigue strength because the amount of solidification shrinkage and entrapped gases is reduced by the injection of partially solidified mixtures. The fatigue strength of SSM specimen in T6 temper can vary between 60 MPa for low solid fraction (25%) and 140 MPa for solid fraction of 60% and an α-Al globule size of 38 μm [11].

For conventionally cast specimens, shrinkage cavities have been most frequently observed at the crack initiation sites [4,5,8,12–14]. In contrast, in semi-solid molding, oxide films are often found at crack initiation sites [7]. Although it is generally accepted that the reduction of fatigue life is a function of the defect size, there is no consensus on the critical defect size that affects the cast aluminum alloy fatigue strength. A critical defect size in the range of 25 μm has been proposed by Wang et al. [6] and Buffière et al. [15]. In addition to the casting defects, the influence of intrinsic microstructural features, such as grain size, secondary dendrites arm spacing (SDAS) and eutectic silicon morphology, on the alloy fatigue strength is not clear. There is no obvious correlation between microstructure, static properties and fatigue properties [12]. For example, heat treatment modifies the eutectic silicon morphology and the alpha phase hardness and has a strong influence on the yield strength of Al–Si–Mg alloys but it was found to have a limited effect on the alloy fatigue strength [3,5,8]. It is thought that the influence of defects prevails over the influence of intrinsic microstructural features. Nevertheless, in defect free specimens, the microstructural constituents play a role in fatigue crack nucleation and long crack propagation. Crack nucleation has been observed at the surface of eutectic silicon particles [2,14,16,17], or at intermetallic particles [2] and at persistent slip bands (PSB) [6,16,18]. The morphology of the alpha phase and of the eutectic silicon particles was also found to influence the crack propagation threshold in a study carried out on PM and SSM cast specimens [19]. However, the correlation between fatigue strength and microstructure has not yet been clearly interpreted in terms of specific damage mechanisms for conventionally cast and rheocast aluminum alloy 357.

* Corresponding author.
E-mail address: myriam.brochu@polymtl.ca (M. Brochu).

0142-1123/$ - see front matter © 2010 Elsevier Ltd. All rights reserved.
doi:10.1016/j.ijfatigue.2010.01.001

This paper presents the results of high cycle fatigue tests performed on aluminum–silicon–magnesium alloy 357 produced by liquid casting and rheocasting. The objective of this work is to identify the microstructural characteristics that have the most significant effect on the alloy fatigue strength. The influence of the defect content, the shape of the eutectic silicon particles, the shape and hardness of the primary phase and the grain size are investigated. Comparative *S–N* curves are presented for six different microstructures. Based on these results, on the fractographic and replica observations, a relationship between the alloy microstructure and its fatigue strength is proposed.

2. Materials and experimental procedure

2.1. Materials

Specimens were prepared from aluminum 357 alloy cast by two different processes. One batch consisting of uniform thickness rectangular plates, 14 millimetres thick, was gravity cast in a permanent mold (PM). Two other samples of rectangular wedge plates, with variable thickness from 16 to 9 millimetres, were rheomolded in the semi-solid state using an industrial pressure die casting machine. Details of the feed stock preparation were presented in a previous publication [20]. For the first batch of SSM plates, the chemical composition of the melt was adjusted as close as possible to the chemical composition of the permanent mold specimens. For the second batch of SSM plates, 25 ppm of strontium was added to the melt to modify the morphology of the eutectic silicon particles. For all batches, approximately 700 kg of A356.2 ingots were first melted in an electric furnace. These ingots had been previously grain refined by an addition of about 0.1% Ti with a Ti/B master alloy in the ratio of 5:1. Once the ingots were melted, magnesium was then added to comply with the 357 alloy composition. In some cases an aluminum-strontium master alloy was also added. Contaminants were removed with a fluxing agent (Promag RI) and argon was also injected in the melt with a rotary impeller. The average chemical compositions of the three batches of plates are given in Table 1.

Some of the PM and SSM-Sr plates were heat treated to T6 temper according to the following procedure: (1) Solution heat treatment in air at 540 °C for 1 h. (2) Warm water quench at 65 °C. (3) Ageing at 155 °C for 8 h. Since solution heat treatment created blisters in many of the SSM-Sr T6 plates, a T5 heat treatment was chosen as an alternative to T6 for some SSM and SSM-Sr plates. The T5 heat treatment sequence consisted of: (1) Extraction from casting mold at 350 °C. (2) Warm water quench at 65 °C. (3) Ageing at 170 °C for 6 h. Six different types of plates were produced: PM-F, PM-T6, SSM-F, SSM-T5, SSM-Sr-T5 and SSM-Sr-T6. All the plates were X-rayed and only the specimens with a quality corresponding to ASTM B108–03 grade B or better (discontinuities smaller than 1 millimetre) were used in this study.

2.2. Microstructural characterization

The microstructure of each type of plate was characterized by metallographic examination of polished and etched sections.

Table 1
Average chemical compositions (wt.%) analysed by optical spectroscopy using ASTM method E 1251(04).

Plates	Weight%							
	Si	Mg	Fe	Ti	Cu	Mn	Zn	Sr[a]	Al
PM	7.80	0.55	0.10	0.09	<0.01	<0.01	<0.01	<0.002	Bal.
SSM	8.10	0.62	0.07	0.12	<0.01	<0.01	<0.01	<0.002	Bal.
SSM-Sr	7.32	0.60	0.07	0.12	<0.01	0.01	<0.01	0.0025	Bal.

[a] Analysed by atomic absorption.

Table 2
Microstructural characteristics of the studied plates.

Plates	Temper[a]	D (μm) [range]	f_α (%) [range]	SDAS (μm) [range]	φ_{sph} (μm) [range]	L_{Si} (μm) [range]
PM	F	[400–1500]	[66–77]	[25–65]	–	[1–40]
PM	T6	[400–1500]	[66–77]	[22–62]	–	[1–40]
SSM	F	[50–350]	[62–75]	–	[5–185]	[1–42]
SSM	T5	[50–350]	[62–75]	–	[8–200]	[1–38]
SSM-Sr	T5	[40–400]	[61–73]	–	[3–230]	[0.5–10]
SSM-Sr	T6	[40–400]	[61–71]	–	[5–200]	[1–15]

[a] F: as-cast, T6: solution heat treated, quenched and peak aged, T5: quenched from the mold and peak aged.

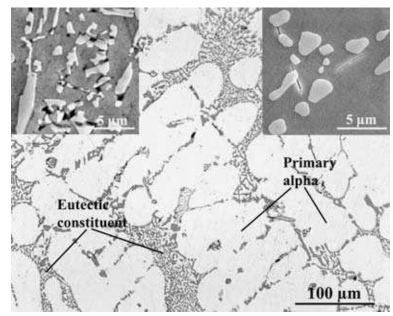

Fig. 1. General view of the microstructure of a PM-F plate. Upper left and right inserts are magnifications of the eutectic constituent of a PM-F and PM-T6 plate respectively.

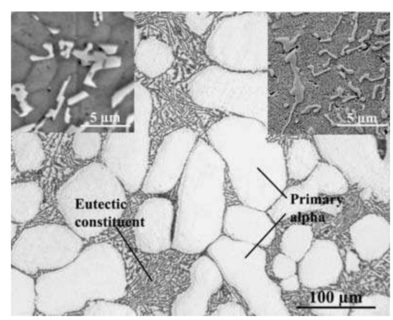

Fig. 2. General view of the microstructure of a SSM-F plate. Upper left and right inserts are magnifications of the eutectic constituent of a SSM-F and SSM-T5 plate respectively.

Transverse and longitudinal specimens showed an equiaxed and homogeneous microstructure for all types of plates. Measurements of microstructural features were carried out using a Nikon optical microscope and Clemex image analysis software. The following characteristics were measured: the grain size (D), the surface fraction of the primary alpha phase (f_α), the secondary dendrite arm spacing (SDAS) for the PM plates, the globule equivalent spherical diameter (φ_{sph}) for the SSM and SSM-Sr plates, and the maximum ferret size of the eutectic silicon particles (L_{Si}). The ranges of the measured microstructural characteristics are given in Table 2.

Typical microstructures of PM-F, SSM–F and SSM-Sr-T5 specimens are shown in Figs. 1–3 respectively. It can be observed that rheomolding produces a more globular alpha phase structure than liquid casting. Magnifications of the eutectic constituent are shown in the upper corners of each figure. PM-F, SSM-F and SSM-T5 plates have a comparable eutectic morphology composed of plate like silicon particles as shown in the left corner of Fig. 1 and the left and right corners of Fig. 2, respectively. The addition of strontium to the SSM-Sr melt resulted in a finer and more rounded eutectic sil-

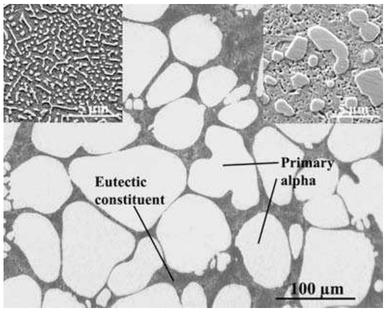

Fig. 3. General view of the microstructure of a SSM-Sr-T5 plate. Upper left and right inserts are magnifications of the eutectic constituent of a SSM-Sr-T5 and SSM-Sr-T6 plate respectively.

Table 3
Average tensile properties and microhardness.

Plates	Temper	σ_y (0.2%) (MPa)	UTS (MPa)	Elongation at fracture (%)	HV (200 g) in alpha phase
PM	F	90	177	7.4	67
PM	T6	264	325	8.3	123
SSM	F	111	213	9.1	64
SSM	T5	182	263	5.8	72
SSM-Sr	T5	185	278	11.7	75
SSM-Sr	T6	288	339	8.8	125

icon particles (left corner of Fig. 3). Higher magnification micrographs of the eutectic constituent after T6 heat treatment are also shown in the right corner of Figs. 1 and 3. It can be seen that the solution heat treatment had a spheroidizing effect on the eutectic silicon particles. PM-T6 and SSM-Sr-T6 specimens have a comparable eutectic morphology.

2.3. Tensile properties and microhardness

The tensile properties were measured on subsize ASTM B557-06 specimens having a square section of 40.32 mm^2. Tests were carried out using a servohydraulic machine and a 25.4 mm extensometer. The average measured properties obtained from three specimens showing no defect on their rupture surfaces are given in Table 3. Specimens with large defects in their reduced section were rejected. These specimens had a considerably lower elongation at fracture and a lower ultimate tensile strength. Five Vickers microhardness measurements of the alpha phase were also carried out on polished cross-sections of each type of plate. The average microhardness values are reported in the last column of Table 3.

The results in Table 3 show that the casting process, the eutectic modification and the heat treatment have a significant effect on the tensile properties. The yield strength of the as-cast rheocast plates (SSM-F) is improved by about 23% when compared to PM-F plates. Addition of an eutectic modifier (Sr) during rheomolding improves the SSM alloy yield strength by 12% in the as-cast condition. It also has a significant effect on the specimen elongation resulting in an improvement of 105%. However, the effect of eutectic modification on the tensile properties is less significant for the T5 heat treated specimens. Precipitation hardening to T6 temper increased the PM and SSM-Sr alloys yield strength and microhardness to their maximum values. Compared to T6 temper, the T5 heat treatment had a smaller effect on the SSM alloy yield strength and microhardness. This is a consequence of the heat treatment procedure. Since there is no solution heat treatment step in the T5 temper, the alpha phase contains less magnesium in solution for the formation of hardening precipitates.

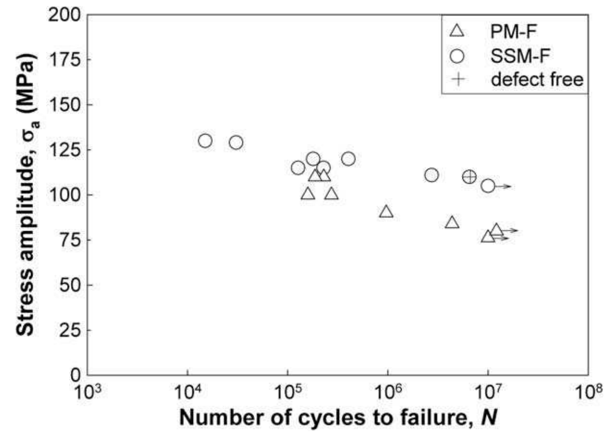

Fig. 4. *S–N* diagram showing the effect of the casting process on aluminum 357-F alloy.

2.4. Fatigue tests

All fatigue tests were carried out on hourglass specimens with a rectangular reduced section of 9.50 mm × 6.35 mm. In a previous study it was shown that using hourglass specimens overestimates the alloy fatigue strength by 15% when compared to results obtained with specimens of uniform test section [21]. Nevertheless, the hour glass specimen geometry was chosen in order to facilitate short crack monitoring. Compared to the uniform section specimens, the hour glass specimen forces crack to nucleate in a small region at the specimen mid-length.

Most specimens were sectioned at the plate mid thickness and along the filling direction but some were also sectioned in the transverse direction. However, no distinguishable trend in the results between the longitudinal and transverse specimens was observed. All specimen surfaces were polished with a 1 μm diamond paste and etched in a solution containing 1% hydrofluoric acid (HF). The axial fatigue tests were carried out at room temperature in laboratory air using a servohydraulic machine at a stress ratio (R) of −1 and a frequency of 20 Hz. The stress amplitudes of the tests were chosen in order to obtain fatigue life between 10^4 and 10^7 cycles.

All tests for which failure occurred outside the specimen reduced section were rejected. The reduced section was limited to 3.5 mm on either side of the sample center line. For this region, the average stress on a plane is within 2% of the nominal stress calculated at the specimen center line. Both crack nucleation and short crack propagation were monitored using silicone replicas taken at periods of 50,000 cycles on the tested specimens that failed at about 10^6 cycles. Crack paths were studied and the crack lengths, c_i, were measured on the replicas using optical microscopy. After testing, the fracture surfaces of the tested specimens were examined in a JEOL JSM-7600 scanning electron microscope. When a defect appeared at the crack initiation site, its area was measured. For complex defect shapes, a smooth perimeter was traced around the defective region and the area of that shape was measured using an image analysis software. For very deep or very shallow defects (e.g. oxide films), the defect area was estimated to be 100 times the square of the defect smallest dimension as proposed by Murakami [22].

3. Results

3.1. Effect of casting process

The results showing the influence of the casting process on the fatigue life of the as-cast alloy are presented in Fig. 4. For both types of specimens, only 65% of the samples failed in the reduced

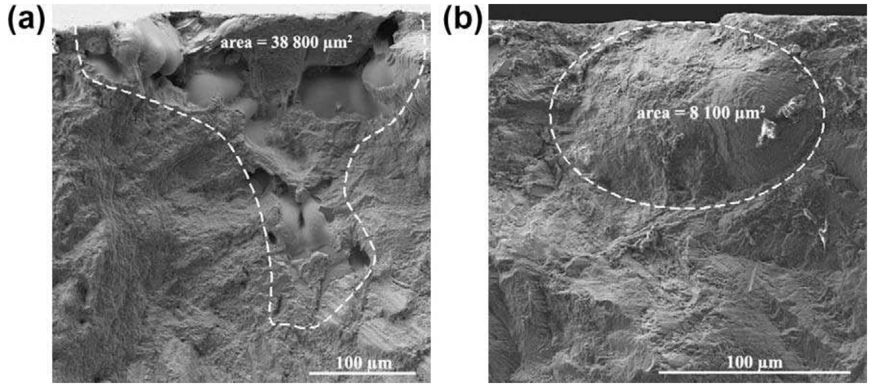

Fig. 5. Crack initiation sites in as-cast specimens at σ_a = 110 MPa. (a) PM-F, N = 229 kilocycles and (b) SSM-F, N = 2 736 kilocycles.

section. This indicates that both molding processes can create defects that are not always detected by X-ray inspection. Only 1 of 14 SSM specimens was defect free and this result is marked with a cross in Fig. 4. The defects observed on the fracture surfaces of the PM specimens were mostly shrinkage cavities, whereas those observed on the fracture surfaces of the SSM specimens were found to be oxide films.

It can be seen from Fig. 4 that, for stress amplitudes at and below 110 MPa, the fatigue life is significantly longer for the SSM specimens than for the PM specimens. This is in accordance with the results published by Gan and Overfelt [23]. Fractographic observations of the four specimens tested at 110 MPa showed that both PM specimens have a shrinkage cavity of comparable size (area of 38,800 μm^2) at their crack initiation site. One specimen fractograph is shown in Fig. 5a. On the other hand, the fatigue crack of one SSM specimen initiated at an oxide film inclusion having an estimated area of 8100 μm^2 (Fig. 5b) and the other SSM specimen tested at 110 MPa is defect free. As expected, the defect free specimen has the longest fatigue life, followed by the other SSM specimen with the smallest defect. The two PM specimens have the largest defects and the shortest fatigue life.

From the fractographic observations it is obvious that smaller defects lead to longer fatigue life as reported in many publications [4–7,13,24]. However, it is not yet possible to conclude that the improved fatigue strength of the SSM alloy is only related to the defect content. The SSM-F and PM-F specimens also have other microstructural differences, specifically, the grain size and the alpha phase particle shape and size.

3.2. Effect of heat treatment

The results in Fig. 6 show the effect of a T6 heat treatment on the fatigue life for the PM alloy. T6 precipitation hardening increases the fatigue strength of the specimens, but not as markedly as the alloy yield strength (see Table 3). At 10^7 cycles, the PM-T6 fatigue strength is only 10 MPa (13%) higher than the PM-F fatigue strength. On the other hand, the PM-T6 specimens have an average yield strength of 264 MPa, which is 193% higher than the average yield strength of the PM-F specimens. Fractographic observations show that, in general, the defects at the crack initiation site of the PM-F and PM-T6 specimens are of comparable size and nature. Only one of fourteen PM-T6 specimens was defect free. For a stress amplitude of 100 MPa, four sets of defect area and fatigue life observations were made: (0.18 mm^2, 159e3 cycles), (0.12 mm^2, 273e3 cycles), (0.02 mm^2, 1.638e6 cycles), and (no defect, 5.288e6 cycles). The microstructural differences between the PM-F and PM-T6 alloys consist of the microhardness of the alpha phase and the morphology of the eutectic silicon particles.

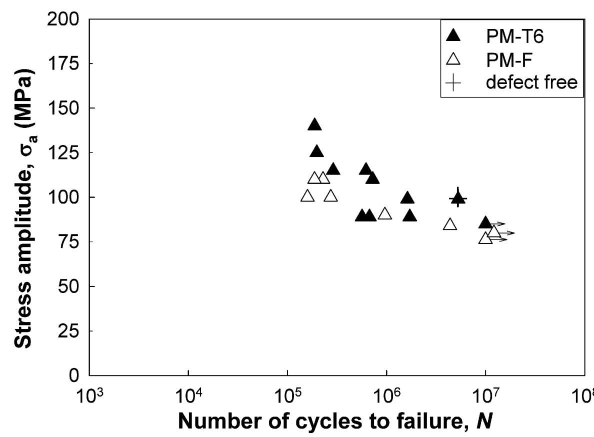

Fig. 6. S–N diagram showing the effect of T6 heat treatment for the PM alloy.

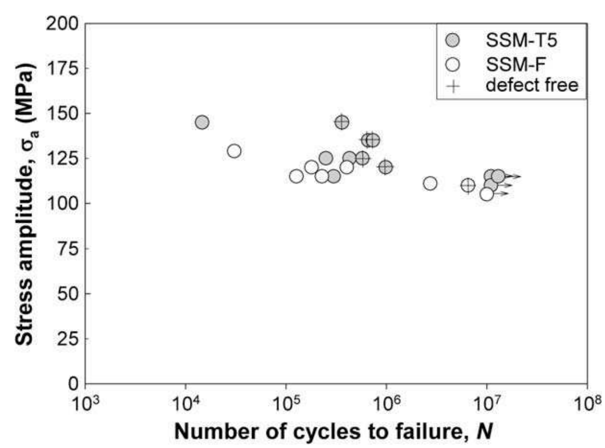

Fig. 7. S–N diagram showing the effect of T5 heat treatment for the SSM alloy.

Results obtained for the SSM specimens, shown in Fig. 7, indicate that heat treatment has a positive but limited effect on the SSM alloy fatigue strength. Although all SSM-T5 specimens, except one, have a longer fatigue life than the SSM-F specimens, their average fatigue strength at 10^7 cycles is only increased by about 10 MPa (106 for SSM-F to 116 MPa for SSM-T5). This is a smaller difference than published by Gan et al. who measured fatigue strengths of 105 MPa and 125 MPa for A357 alloy with F and T5 temper. It can be observed that the heat treated specimens are more often defect free (symbols with a cross) than the as-cast spec-

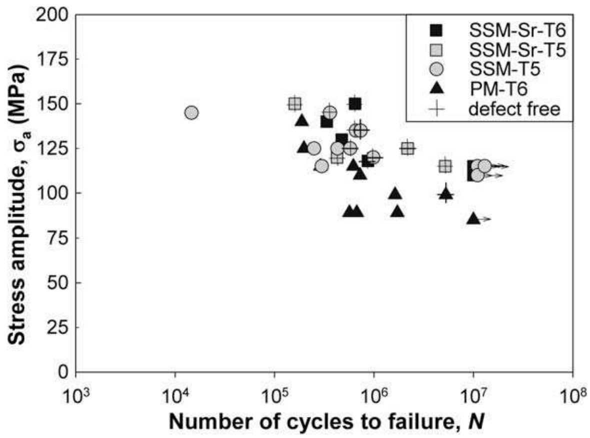

Fig. 8. *S–N* diagram showing the effect of eutectic modification for the SSM alloy.

imens. This difference in defect occurrence between the SSM-F and SSM-T5 specimens and may be of statistical nature. All plates were cast from the same batch but the SSM-F plates were cast first and the SSM-T5 plates were cast last. It is possible that the processing conditions could have improved during the casting process. Beside defects, the only noticeable difference between the SSM-F and SSM-T5 specimens is the microhardness of the alpha phase.

3.3. Effect of eutectic modification

Modification of the eutectic microstructure was investigated by adding 25 ppm of strontium to the melt for the rheomolded SSM-Sr plates. The effect of the eutectic modification on the alloy fatigue strength was compared for the heat treated SSM-Sr-T5 and SSM-T5 specimens. The rejection rate for the tests done on the SSM-Sr-T5 plates was significantly higher than for the other batches where 57% of the tested specimens failed outside the reduced section. On the other hand, most of the valid specimens were defect free (symbols with a cross). This difference in rejection rate between the batches of specimens could not be explained and could be of statistical nature they could also be attributed to a variation in the processing conditions from one batch to another.

In Fig. 8, it can be seen that the results obtained for the SSM-Sr-T5 specimens fall in the scatter band of the results obtained for the SSM-T5 specimens. By comparing the fatigue life of the defect free specimens, no specific trend differentiating the alloys can be seen. Some SSM-Sr-T5 specimens have a longer fatigue life than SSM-T5 specimens but others have a shorter fatigue life. This suggests that eutectic modification does not have a significant effect on the alloy fatigue strength. The fractographic observations shown in Fig. 9 can explain these findings. Crack nucleation and short crack propagation did not occur in the silicon rich eutectic region but rather in the primary alpha phase. For the specimens studied, the most common crack initiation sites that were observed, excluding defects, are the persistent slip bands found in the alpha phase. Wang et al. [6] made similar observations for a A356-T6 PM alloy.

Comparison of the results obtained for the SSM-Sr-T5 with SSM-Sr-T6 alloys also confirms that the size of the silicon particles do not have a significant effect on the alloy fatigue strength. The SSM-Sr-T6 results are in the same scatter band as the results obtained for the SSM-Sr-T5, even though the silicon particles in the first alloy are larger than in the second. The same trend was observed by Basner [25] for A357 alloy.

4. Discussion

4.1. Fatigue strength

The fatigue strength at 10^7 cycles, presented in Figs. 4 and 6–8 were calculated using Basquin's power law, $\sigma_a = \sigma'_f N^{-b}$, where σ'_f is the fatigue strength coefficient and b the fatigue strength exponent. The equation parameters as well as the fatigue strengths at $N = 10^7$ cycles are presented in the first, third and second column of Table 4 respectively. For the SSM-T5, SSM-Sr-T5 and SSM-Sr-T6 specimens, the results were analysed globally since they follows the same trend shown previously (Fig. 8). The comparison of the calculated fatigue strengths shows that the rheomolded and heat treated specimens are the most resistant to high cycle fatigue. SSM-T5 alloy has a fatigue strength that is 31 MPa (38%) higher than the PM-T6 alloy. This is significant because the T6 heat treatment is more costly than the T5 heat treatment and it can cause other quality problems (such as blisters) in parts cast under pressure. In the as-cast condition, rheomolding also increases alloy fatigue strength with an improvement of 28 MPa (36%) compared to permanent molding.

4.2. Influence of defects

Defect free specimens were also analysed using Basquin's equation in order to identify the effect of the defects on fatigue strength improvement of the SSM specimens. For each set of data, the same fatigue strength exponent, *b*, obtained in section 4.1 was used but the fatigue strength coefficient was adjusted to fit only the results of the defect free specimens. An example of the proposed regressions is given in Fig. 10 for the PM-T6 alloy. The fatigue strength coefficient of the defect free specimens, σ'_{th}, is given in the fifth column of Table 4 together with the theoretical fatigue strength at 10^7

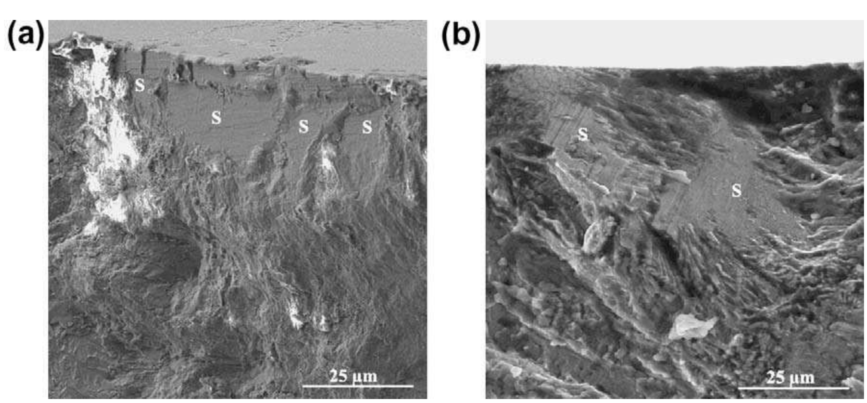

Fig. 9. Crack initiation sites in SSM specimens tested at σ_a = 120 MPa. (a) SSM-T5, N = 983 kilocycles, (b) SSM-Sr-T5, N = 425 kilocycles (S = stage I shear crack).

Table 4
Basquin equation parameters and fatigue strength for alloy 357 with different microstructures.

	All valid results		b	Defect free specimens	
	σ'_f MPa	Fatigue strength at 10^7 cycles		σ'_{th} MPa	Fatigue strength at 10^7 cycles
PM-F	261	78	0.075	290	87
PM-T6	366	82	0.093	415	93
SSM-F	172	106	0.030	178	110
SSM-T5, SSM-Sr-T5, SSM-Sr-T6	237	113	0.046	252	120

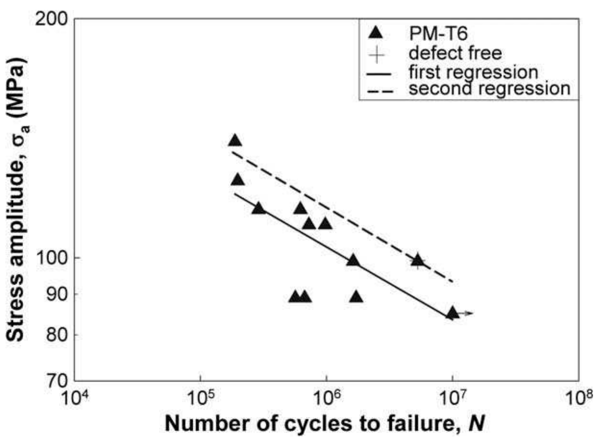

Fig. 10. Example of the regressions applied to the overall *S–N* results (first regression) and to the defect free results (second partial regression).

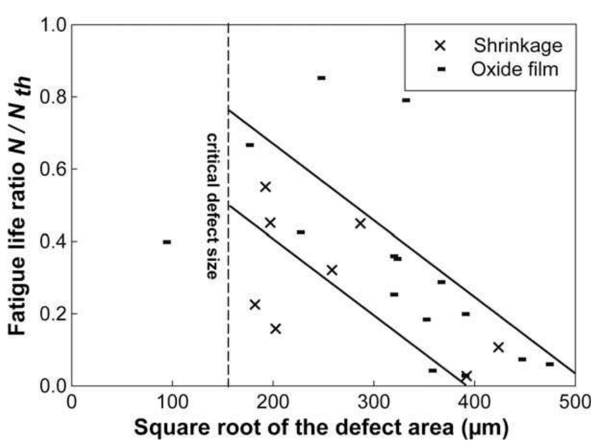

Fig. 11. Influence of the defect size on the fatigue life ratio of the SSM and the PM specimens.

cycles, calculated using this second equation. The comparison of the fatigue strength given in the columns 3 and 6 of Table 4 shows that the difference in fatigue strengths between the PM and SSM alloys is smaller for the defect free specimens. For the heat treated specimens, the difference in fatigue strength is reduced from 38% to 29% when considering the results of defect free specimens only. As a consequence, about 10% of fatigue strength improvement can be explained by a difference in defect content (number, size, nature, location) found in the specimens.

A graph showing the specimen fatigue life ratio as a function of the square root area of the defect at the crack initiation site is shown in Fig. 11 illustrating the effect of the size and the nature of the defects on the results. The fatigue life ratio, for a given stress amplitude, is defined by the number of cycles to failure (N) divided by the theoretical fatigue life calculated for a defect free specimen (N_{th}). The theoretical fatigue life is calculated using the partial regression applied to the defect free specimens as described previously. In Fig. 11, no distinction is made between the alloys but different symbols are used to distinguish the specimens with a shrinkage cavity from the specimens with an oxide film. The results show that there is a single and linear relation between the fatigue life ratio and the square root of the defect area. This relation is independent of the alloy processing condition and of the nature of the defect. This finding is different from the results of Davidson et al. [7] and Wang et al. [6] who showed that oxide defects have a smaller effect on fatigue life than pores of the same area. In Fig. 11, the two results located in the upper portion of the graph are associated with oxide films located at about 100 μm from the specimen surface. The results clearly showed that a lower fatigue life ratio was measured for specimens with shrinkage cavities or inclusions at the surface of the specimens. This confirms that the defect position is an additional a parameter that should be considered to better predict fatigue life as proposed by Seniw [26].

Even though defects size ranges overlapped for all six groups, there were more defect free SSM specimens than PM specimens as shown in Figs. 4 and 8. According to our interpretation, rheomolding improves the alloy fatigue strength because it reduces the volume fraction of defects which is in accordance with the conclusions of Wang et al. [27].

Nevertheless, a significant difference between the fatigue strength of the defect free PM and SSM specimens in the as-cast and heat treated conditions is still evident. Apparently, other features can have an influence on the alloy fatigue behaviour. Based on the microstructural characteristics given in Table 2, the SSM-F alloy has a smaller grain size and a more globular alpha phase than the PM-F alloy. The same microstructural differences exist between the heat treated SSM and the PM alloys.

In addition, the results in Fig. 11 show the existence of a vertical asymptote at about 155 microns where defects smaller than 155 microns were seldom observed at the fracture surfaces of the specimens. This could indicate that the range of the critical defect sizes for the 357 alloy is larger than the value proposed by Wang et al. [6]. According to these authors the critical defect size should be in the range of the SDAS in coarse microstructures (SDAS > 40 μm) whereas in fine microstructures (SDAS < 40 μm) it should be in the range of the grain size. For the alloys of this study, 155 μm is larger than both the SDAS and the alpha globules spherical diameter but smaller than the alloy grain size.

4.3. Short crack growth and microstructure

The results of this study showed that rheomolding has a beneficial effect on the fatigue strength of 357 alloy and that this effect is not totally explained by the reduction in defect content. A more detailed analysis of the interactions between fatigue cracks and the alloy microstructure was therefore undertaken. The observation of replicas by optical microscopy was carried out to study the crack nucleation mechanism as well as the crack propagation path. Using the replicas, the projected normal lengths of each side of the crack were measured from the initiation site (marked by a star) to the left end of the crack (c_1) and to the right end (c_2) as shown in Fig. 12. Tracking the two crack ends separately shows the crack growth deceleration better than tracking the full crack length ($2c = c_1 + c_2$). When one end of the cracks is blocked at a microstructural barrier, the other end of the cracks can still propagate in the absence of such barriers.

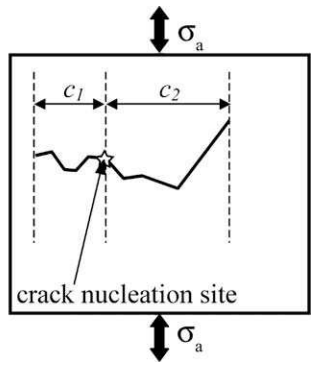

Fig. 12. Projected crack lengths to the left side (c_1) and to the right side (c_2) of the nucleation site.

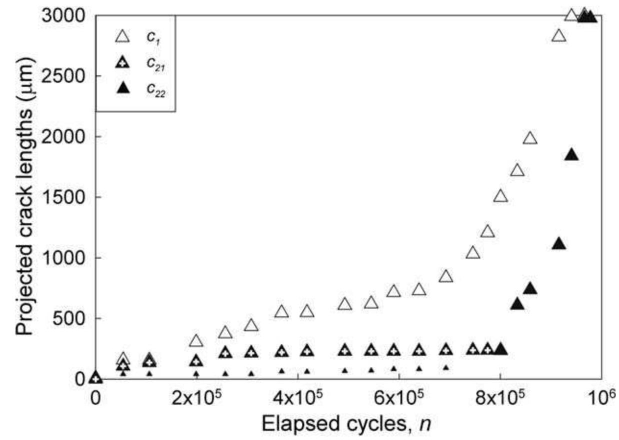

Fig. 14. Short crack propagation in a PM-T6 specimen, σ_a = 110 MPa and N = 978 kilocycles.

The path of a crack observed in a PM-T6 alloy is shown in Fig. 13 and a graphical representation of the crack size as a function of the elapsed cycles (n) is given in Fig. 14. A 107 μm long crack was observed after 54 kilocycles (6% of the total fatigue life). The replica taken before the test (Fig. 13a), showed a discontinuity in the eutectic region that was identified as the initiation site. Fractographic observations showed that this discontinuity is a small shrinkage cavity with an area of 3750 μm^2. A stage I crack grew to the left and to the right of this casting defect on a crystallographic plane oriented at about 55° from the loading direction (Fig. 13b). Stage I identifies a crack growing along maximum shear planes. It can be seen from Figs. 13 and 14 that the right side of the crack, c_{21}, grew rapidly without changing direction and without any deceleration, even though it crossed many alpha phase cells separated by clusters of silicon particles. These alpha cells most probably belong to the same dendrite and consequently have an unique crystallographic orientation which results in a relatively weak barrier to short crack propagation. After propagating for 240 μm in stage I, the right end of the crack stopped at a cluster of silicon particles, comparable to the other clusters encountered previously (Fig. 13c). At this point, the propagation of c_{12} was completely arrested and never proceeded to stage II. It is believed that c_{12} encountered a new grain oriented unfavourably for slip propagation. After about 500 kilocycles (50% of total life duration) a new crack grew from the original nucleation site and propagated to the right as shown in Fig. 13d. This new branch, identified c_{22}, started its propagation at stage II and was never subjected to crack growth deceleration until specimen failure.

The crack propagation to the left, c_1, was also subjected to crack growth deceleration as seen in Fig. 14. A first significant deceleration was observed during the crack transition from stage I to stage

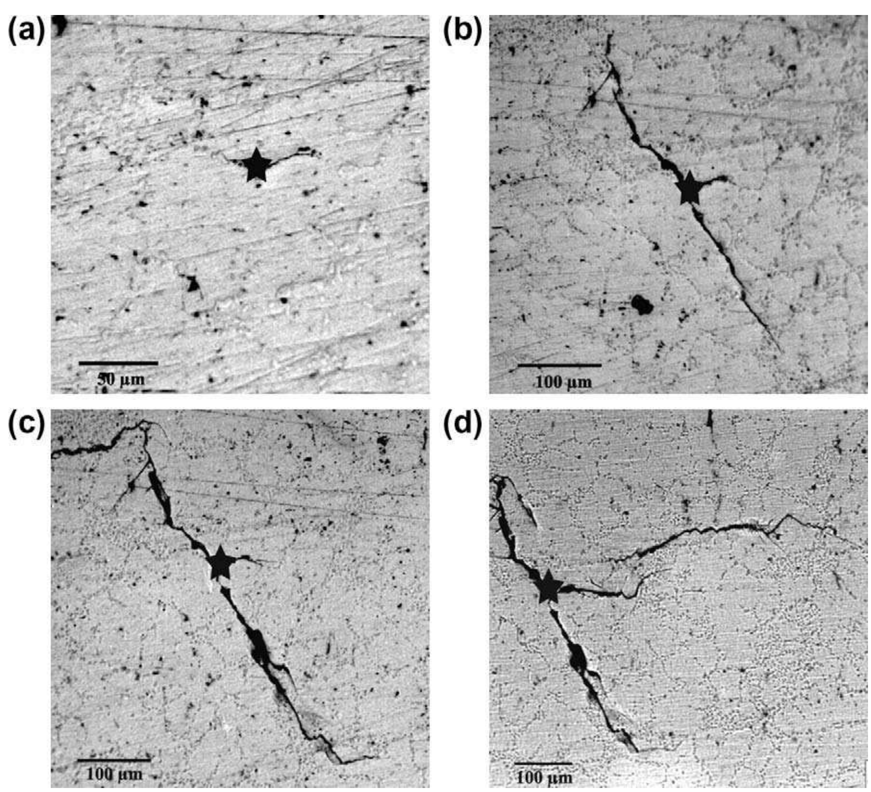

Fig. 13. Propagation path of the right side of the crack, c_2 in Fig. 14; specimen axis is vertical. (a) n = 0 cycles, c_1 = 10 μm, c_{21} = 0 μm, c_{22} = 40 μm, (b) n = 54 kilocycles, c_1 = 158 μm, c_{21} = 107 μm, c_{22} = 40 μm, (c) n = 545 kilocycles, c_1 = 620 μm, c_{21} = 230 μm, c_{22} = 70 μm and (d) n = 834 kilocycles, c_1 = 1713 μm, c_{21} = 240 μm, c_{22} = 610 μm.

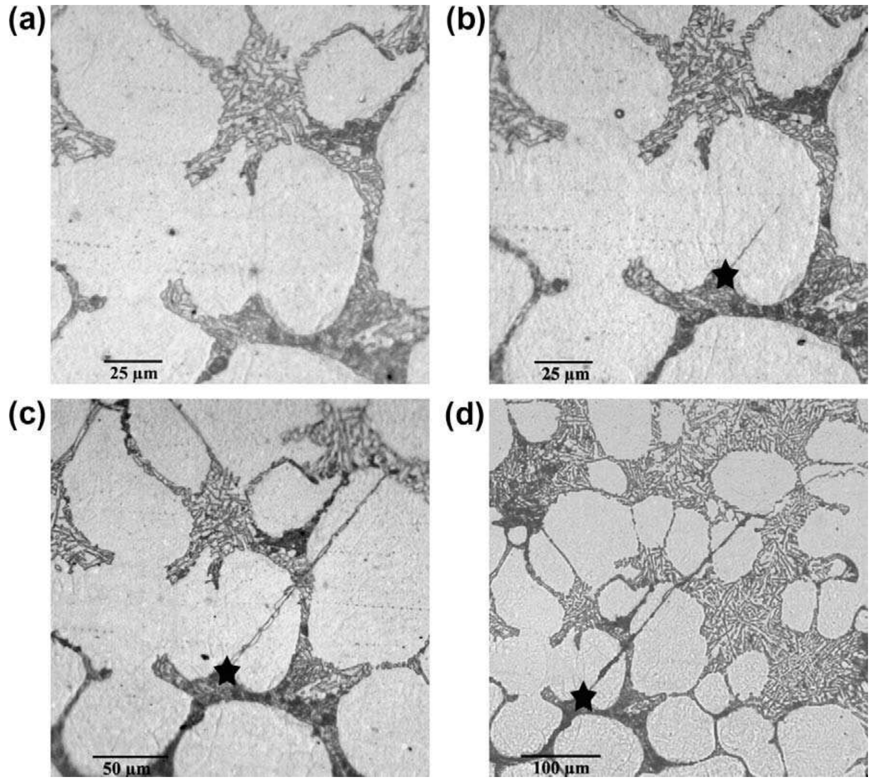

Fig. 15. Propagation path of the right side of the crack, c_2 in Fig. 16; specimen axis is vertical. (a) $n = 0$ cycles, $c_1 = 0$ µm, $c_2 = 0$ µm, (b) $n = 389$ kilocycles, $c_1 = 0$ µm, $c_2 = 30$ µm, (c) $n = 445$ kilocycles, $c_1 = 175$ µm, $c_2 = 115$ µm and (d) $n = 774$ kilocycles, $c_1 = 548$ µm, $c_2 = 387$ µm.

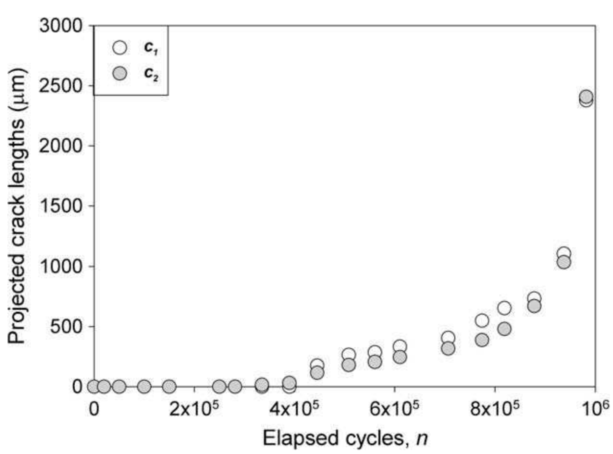

Fig. 16. Short crack propagation in a SSM-T5 specimen, $\sigma_a = 120$ MPa and $N = 983$ kilocycles.

II that occurred at $n = 54$ kilocycles and at a projected length of 160 µm. This transition probably occurred when the crack tip encountered a new grain. A cluster of silicon particles was observed at the transition site. The growth of the crack to the left decelerated three more times at projected lengths of about 540 µm, 600 µm and 730 µm from the initiation site. When considering both sides, the crack progressed in stage I for a total length of 400 µm ($c_1 = 160$ µm; $c_{21} = 240$ µm). Its last deceleration occurred at 970 µm ($c_1 = 730$ µm; $c_{21} = 240$ µm). These lengths are comparable to the alloy grain size (Table 2).

The same analysis was carried out for the SSM-T5 alloy specimen. Figs. 15 and 16 show crack initiation from a persistent slip band in the alpha phase after about 390,000 cycles, which is 40% of the specimen total fatigue life. For this particular test, no defect was observed on the fracture surfaces at the nucleation site (Fig. 9a). Subsequently, the right side of the crack (c_2) propagated within the alpha phase in stage I – on a plane of maximum shear stress oriented at 45° from the loading direction (Fig. 15b). The crack continued its crystallographic propagation in a second globule (Fig. 15c) which is probably within the same grain since no crack path deviation and no crack growth deceleration was observed. However, a crack growth deceleration was observed at a projected length of 180 µm (Fig. 16) when c_2 reaches the end of the second globule ($N \approx 500{,}000$ cycles; replica 15c). At this point, the crack is gradually deflected to reach a crack opening mode I (stage II) as shown in Fig. 15d. The crack deflection was not drastic and could be attributed to the fact that the adjacent grain had a small misorientation angle with the initial grain. At a length of 500 µm, the right end of the crack was clearly in stage II. Pure stage I propagation occurred during the first 180 µm (Fig. 15c), which is within the range of the SSM grain size (Table 2).

The propagation of the left side of the crack, c_1, originated within the eutectic constituent on a plane oriented at 45° from the specimen axis. After propagating for about 50 µm, the crack path deviated and stage II propagation began. When the crack front reached a first globule of alpha phase, at about 100 µm from the nucleation site, no significant crack growth deceleration (Fig. 16) nor any significant crack path deviation was observed. The end of the crack reached another alpha phase globule at 240 µm from the initiation site. Between 240 µm and 650 µm the crack grew in a stage I like mode changing direction from one globule of alpha phase to another. On a macro scale, the crack path remained normal to the specimen axis. It can be seen from Fig. 16 that the crack propagation rate of c_1 is irregular until it reached 650 µm. It is possible that the encountered alpha phase globules were not of the same grain which created barriers to crack propagation.

The analysis of the crack nucleation site, the crack path and the crack growth rate given in Figs. 13–16, identifying the interactions between the fatigue crack and the microstructure. It is evident that the number of cycles for crack initiation is significantly reduced in the PM specimen because the crack nucleated at a defect. The PM-T6 specimen tested at 110 MPa, which is 42% of the alloy yield strength, even though crack in the specimen initiated rapidly, 50% of the specimen life elapsed before both sides of the crack propagated in stage II. During stage I propagation, a significant portions of crack growth decelerations were associated with important crack path deviations. This indicates that microstructural barriers create discontinuities in the local slip orientation which impede stage I crack propagation. For the SSM-T5 specimen tested at 120 MPa, which is 65% of the alloy yield strength, 83% of fatigue life had elapsed before both sides of the crack propagated in stage II. Crack growth decelerations comparable to that of the PM specimens were observed. For both the PM-T6 and SSM-T5 specimens, it was observed that a crack can have a continuous stage I propagation mode across adjacent alpha phase cells. Consequently, alpha phase cells within the same grain (i.e. secondary dendrite arms) are not necessarily important microstructural barriers. The results show that grain boundaries can be considered to be more efficient microstructural barriers because they interrupt the lattice continuity of the alpha phase where crystallographic propagation takes place. On this basis, the improved fatigue strength of SSM alloys of this study is attributed to the decreased defect volume fraction (especially shrinkage cavities) and to the smaller grain size of the rheocast microstructure. It would therefore be beneficial for both the PM and SSM alloys to have smaller grains.

5. Conclusions

This experimental study demonstrated the influence of specific microstructural characteristics on the fatigue strength of 357 alloy. Specimens with six different microstructures were analysed from permanent mold and rheomolded castings, with and without eutectic modification and for different heat treatments. All microstructures were characterized and subjected to axial fatigue tests under full reversing load conditions. Even though defects found in specimens displayed some dispersion, the results showed that:

- Rheomolding increases the mean as-cast alloy fatigue strength (10^7 cycles) from 78 MPa to 106 MPa.
- Heat treating the permanent mold specimens to T6 temper improved their fatigue strength by 5% while it increased their yield strength by 193%.
- Heat treating the semi-solid plates to T5 temper improved their fatigue strength by 7% and no additional gain was obtained by tempering to T6.
- 357 alloy is more fatigue resistant when it is rheomolded and T5 heat treated when compared to permanent mold castings with T6 heat treatment.
- Eutectic modification of the semi-solid alloy using small amounts of Sr addition did not improve the fatigue strength but doubled the elongation at fracture.

The fatigue strength results combined with fractographic and microstructural observations led to the following conclusions:

- For a specific microstructure, the fatigue life is significantly reduced when a crack initiates at a defect.
- Cracks in PM specimens most often initiate at shrinkage cavities while cracks in SSM specimens most often initiate at oxides inclusions. Both types of defects are detrimental to fatigue strength.
- Even though the SSM specimens are more defect free than the PM specimens, the defect content can not entirely explain the difference in fatigue strength between the microstructures investigated.
- Grain size appears to be a microstructural feature that has a significant effect on the alloy fatigue strength because grain boundaries are efficient microstructural barriers to stage I crack propagation.

Based on these conclusions, it is reasonable to propose that the smaller grains of the SSM alloy microstructures improved fatigue strength because it created more obstacles to short crack propagation. This could explain why, for a given stress amplitude, defect free SSM specimens have a longer fatigue life than defect free PM specimens. To support these conclusions, future research efforts should be oriented toward the quantification of the alpha phase lattice misorientation angle that is associated with a crack growth deceleration. It would also be interesting to compare the fatigue strength of PM and SSM alloys having comparable grain size.

Acknowledgements

Contributions from CRSNG, FQRNT, REGAL and Rio-Tinto Alcan for funding this research are acknowledged.

References

[1] Knott JF, Bowen P, Luo J, Jiang H, Sun HL. The structural integrity of cast aluminium automotive components subjected to fatigue loads. Mater Sci Forum 2000;331–337:1401–12.
[2] Shiozawa K, Tohda Y, Sun S-M. Crack initiation and small fatigue crack growth behaviour of squeeze-cast Al–Si aluminum alloys. Fatigue Fract Eng Mater Struct 1997;20:237–47.
[3] Davidson CJ, Griffiths JR, Machin AS. The effect of solution heat-treatment time on the fatigue properties of an Al–Si–Mg casting alloy. Fatigue Fract Eng Mater Struct 2002;25:223–30.
[4] Yi JZ, Gao YX, Lee PD, Flower HM, Lindley TC. Scatter in fatigue life due to effects of porosity in cast A356–T6 aluminum–silicon alloys. Metall Mater Trans A 2003;34A:1879–90.
[5] Couper MJ, Neeson AE, Griffiths JR. Casting defects and the fatigue behaviour of an aluminium casting alloy. Fatigue Fract Eng Mater Struct 1990;13:213–27.
[6] Wang QG, Apelian D, Lados DA. Fatigue behavior of A356–T6 aluminum cast alloys Part I. Effect of casting defects. J Light Met 2001;1:73–84.
[7] Davidson CJ, Griffiths JR, Badiali M, Zanada A. Fatigue properties of a semi-solid cast Al–7Si–0.3Mg–T6 alloy. Metall Sci Technol 2000;18:27–31.
[8] Skallerud B, Iveland T, Harkegard G. Fatigue life assessment of aluminum alloys with casting defects. Eng Fract Mech 1993;44:857–74.
[9] Chen W, Zhang B, Wu T, Poirier D, Sung P, Fang QT. Microstructure dependence of fatigue life for A356.2. In: Das SK, (Ed.), Proceedings of the TSM annual meeting, San Antonio (TX); 1998.
[10] Caton MJ, Jones JW, Mayer H, Stanzl-Tschegg SE, Allison JE. Demonstration of an endurance limit in cast 319 aluminum. Metall Mater Trans A 2003;34A:33–41.
[11] Brochu M, Verreman Y, Ajersch F, Bucher L. Fatigue behavior of semi-solid cast aluminum: a critical review. Solid State Phenom: Diffus Defect Data Part B 2008;141–143:725–30.
[12] Stanzl-Tschegg SE, Mayer HR, Beste A, Kroll S. Fatigue and fatigue crack propagation in AlSi7Mg cast alloys under in-service loading conditions. Int J Fatigue 1995;17:149–55.
[13] Ammar HR, Samuel AM, Samuel FH. Porosity and the fatigue behavior of hypoeutectic and hypereutectic aluminum–silicon casting alloys. Int J Fatigue 2008;30:1024–35.
[14] Zhang B, Poirier DR, Chen W. Microstructural effects on high-cycle fatigue-crack initiation in A356.2 casting alloy. Metall Mater Trans A 1999;30A:2659–66.
[15] Buffiere J-Y, Savelli S, Jouneau PH, Maire E, Fougères R. Experimental study of porosity and its relation to fatigue mechanisms of model Al–Si7–Mg0.3 cast Al alloys. Mater Sci Eng A 2001;316:115–26.
[16] Murakami Y. Influence of Si-phase on fatigue properties of aluminium alloys. In: Murakami Y, editor. Metal fatigue: effects of small defects and nonmetallic inclusions. Oxford: Elsevier; 2002. p. 217–39.
[17] Han S-W, Kumai S, Sato A. Effects of solidification structure on short fatigue crack growth in Al–7%Si–0.4%Mg alloy castings. Mater Sci Eng A 2002;332:56–63.
[18] Caton MJ, Jones JW, Boileau JM, Allison JE. The effect of solidification rate on the growth of small fatigue cracks in a cast 319-type aluminum alloy. Metall Mater Trans A 1999;30A:3055–68.

[19] Lados DA, Apelian D. Fatigue crack growth mechanisms during dynamic loading of conventionally and SSM cast aluminum components. In: Apelian D, Alexandrou A, Georgiou G, Jorstad J, Makhlouf M, editors. Proceedings of the 8th international conference on semi-solid processing of alloys and composites. Limassol; 2004.

[20] Doutre D, Langlais J, Roy S. The seed process for semi-solid forming. In: Apelian D, Alexandrou A, Georgiou G, Jorstad J, Makhlouf M, editors. Proceedings of the 8th international conference on semi-solid processing of alloys and composites. Limassol; 2004.

[21] Brochu M, Verreman Y, Ajersch F, Charest N. Fatigue testing of a cast aluminum alloy: experimental challenges. In: Proceedings of the 12th international conference on fracture, National Research Council Canada (Ed.), Ottawa; 2009.

[22] Murakami Y. Stress concentration. In: Murakami Y, editor. Metal fatigue effects of small defects and nonmetallic inclusions. Oxford: Elsevier; 2002. p. 11–24.

[23] Gan YX, Overfelt RA. Fatigue property of semisolid A357 aluminum alloy under different heat treatment conditions. J Mater Sci 2006;41:7537–44.

[24] Linder J, Axelsson M, Nilsson H. The influence of porosity on the fatigue life for sand and permanent mould cast aluminium. Int J Fatigue 2006;28:1752–8.

[25] Inguanti PC. Cast aluminum fatigue property/microstructure relationships. In: Proceedings of the 17th national SAMPE technical conference, Society for the Advancement of Material and Process Engineering (Eds.), Kiamesha Lake (NY); 1985.

[26] Basner TG. Ph.D. thesis. Material engineering, University of Michigan; 2001.

[27] Seniw ME, Fine, ME, Chen EY, Meshii, M, Gray J. Relation of defect size and location to fatigue failure in Al alloy A356 cast specimens. In: Soboyejo, WO, Srivatsan, TS. (Eds.), Proceedings of the symposium on high cycle fatigue of structural materials, Indianapolis (IN); 1997.